

Particle simulation of vibrated gas-fluidized beds of cohesive fine powders

Sung Joon Moon, I. G. Kevrekidis, and S. Sundaresan*

*Department of Chemical Engineering & Program in Applied and Computational Mathematics
Princeton University, Princeton, NJ 08544*

We use three-dimensional particle dynamics simulations, coupled with volume-averaged gas phase hydrodynamics, to study vertically vibrated gas-fluidized beds of fine, cohesive powders. The volume-averaged interstitial gas flow is restricted to be one-dimensional (1D). This simplified model captures the spontaneous development of 1D traveling waves, which corresponds to bubble formation in real fluidized beds. We use this model to probe the manner in which vibration and gas flow combine to influence the dynamics of cohesive particles. We find that as the gas flow rate increases, cyclic pressure pulsation produced by vibration becomes more and more significant than direct impact, and in a fully fluidized bed this pulsation is virtually the only relevant mechanism. We demonstrate that vibration assists fluidization by creating large tensile stresses during transient periods, which helps break up the cohesive assembly into agglomerates.

PACS numbers:

I. INTRODUCTION

It is well known that fine, cohesive particles cannot be fluidized easily. [1, 2] When fluidization by an up-flow of gas is attempted, assemblies of such particles tend to lift up as a plug and only form ratholes and cracks through which the fluid escapes. Attractive interparticle forces frequently arise as a result of capillary liquid bridges or van der Waals forces. A variety of techniques to achieve smooth fluidization of such particles have been explored in the literature. When the cohesion arises from van der Waals forces, as in the case of Geldart type C particles which are typically $30\ \mu\text{m}$ or smaller in size, [1] coating with hard nanoparticles [3] or an ultrathin film [4] can weaken the attraction between the bed particles, thus enabling smooth fluidization. Alternate approaches to facilitate fluidization include causing agglomerate break-up through a secondary supply of energy using mechanical vibration, [5, 6, 7, 8, 9, 10, 11, 12] acoustic waves [13, 14, 15] or an oscillating magnetic field. [16] Such approaches have been shown to be effective even for beds of nanoparticles. [11] In the present study, we are concerned with some aspects of the mechanics of vibrated fluidized beds of cohesive particles.

Vibrated layers of granular materials have been studied extensively in the literature and formation of patterns in shallow granular layers is now well known. [17, 18] Mixing and segregation in such vibrated beds have also received considerable attention. [19, 20, 21] The motion of large intruders in vibrated beds, leading to the well-known Brazil nut and reverse Brazil nut effects, [19, 22] has also received much attention in the literature, where experimental measurements suggest a non-negligible influence of the interstitial gas on the observed flow patterns. [23, 24] In general, the deeper the bed and/or the

smaller the bed particles, the greater the influence of the interstitial gas phase on the dynamics of the assembly of particles.

In vibrated fluidized beds, where vibration is supplemented with a fluidizing gas flow (or *vice versa*), the importance of the interstitial gas is obvious as the drag due to the gas flow supports a substantial portion of the weight of the particles. Vibrated fluidized beds have found many applications in industrial practice (e.g., see an article by Squires [25]). Understanding the manner in which the vibration aids the fluidization process is important both for macroscopic analysis of vibrated fluidized beds and for detailed interrogation of agglomerate size distribution and mixing at the agglomerate and particle scales.

Predicting the minimum fluidization velocity of a vibrated fluidized bed (of cohesive particles) is perhaps the simplest quantitative, macroscopic analysis problem one can think of. This indeed has been a subject of many investigations [7, 8, 9, 11, 26, 27, 28, 29] and different approaches have been proposed in the literature to incorporate the effect of vibration on the overall force balance used to determine the minimum fluidization velocity. Musters and Rietema [26] suggested that additional terms need to be included in the force balance relation in order to account for the increased pressure drop due to cohesion. They included additional terms for interparticle forces as well as wall friction. Liss *et al.* [27] proposed an additional term to account for the effect of cohesion arising from liquid bridges. Wank *et al.* [8] showed that the agglomerate size decreases as the vibration intensity increases, and studied the effect of the pressure on the minimum fluidization velocity. Erdész and Mujumdar [28] developed a theory which includes the effect of vibration in the prediction of the minimum fluidization velocity; they found that the pressure drop decreased with increasing vibration intensity in their experiments with various particles in the range 0.15-2.75 mm. However, Tarisin and Anuar [29] found the opposite trend in their study of vibrofluidization of particles of

*Corresponding author: sundar@princeton.edu; 609-258-4583 (tel); 609-258-0211 (fax).

15 μm to 34 μm , and others [7, 9, 11] found no appreciable dependence on the vibration intensity with particles of range 12 nm through 100 μm .

Such conflicting reports stem from our limited understanding of the manner in which the vibrating boundary interacts with the assembly of particles in the bed. One can readily envision at least two modes of interaction: (a) When the effect of the interstitial gas on particle motion is of negligible importance, the vibrating base plate clearly imparts impulse to the particle assembly periodically only through direct collisions. (b) When gas-particle drag is non-negligible, a periodically varying pressure field can be expected to develop in the bed, and the base plate interacts with the bed particles indirectly by driving these pressure pulsations as well. The relative importance of these two contributions can be expected to depend on the bed depth, particle size, and the superficial velocity of the fluidizing gas; however, quantitative estimates are unavailable.

At a more detailed level, it is readily apparent that vibration results in the formation of small agglomerates which are more amenable to fluidization, yet how such small agglomerates are formed is not understood. A clear understanding of this mechanism is an important first step in any effort to capture the effect of vibration on the dynamics of agglomerates (e.g., in a population-balance-type model for vibrated fluidized beds). At first glance, one may speculate that vibration drives vigorous collisions between agglomerates, which in turn causes their break-up; but it is not known if this is indeed the dominant mechanism.

In the present study, we have examined the interaction of the vibrating base plate with a bed of particles through detailed simulations. We will demonstrate that as the fluidizing gas velocity is increased, the interaction with the boundary through pressure pulsation becomes more and more dominant and that above the minimum fluidization conditions, the interaction occurs almost exclusively through pressure pulsations. We will also show that the large tensile stress induced by the vibration is a more important mechanism (than vigorous collisions between agglomerates) in causing the break-up of the cohesive particle assembly.

The dynamic behavior of gas fluidized beds containing a large number of particles has been widely examined in the literature through two-fluid models. [30, 31, 32] This approach requires closure relations for gas-particle interactions and the stresses. Considerable progress has been made in developing and validating the closures for assemblies of non-cohesive particles, [30, 31, 32] but not for the case of cohesive materials. Accurate two-fluid model boundary conditions that capture the effect of vibrating boundaries are also unavailable. Furthermore, the two-fluid model approach is not well suited for investigation of the mechanism of agglomerate break-up. For these reasons, we model vertically vibrated gas fluidized beds of fine powders using a hybrid scheme, where the solid phase is treated as discrete spherical particles, fol-

lowing the so-called discrete element method (DEM; or soft-sphere molecular dynamics), [33] while the gas phase is treated as continuum, following the volume-averaged hydrodynamics just like in a two-fluid model. [31, 32] This DEM-based hybrid approach was proposed by Tsuji *et al.* [34] in their simulation of two-dimensional (2D) fluidized beds, and it has been subsequently refined by others. [35, 36] Recently, this model has been used to study fluidized beds of Geldart A particles, [37] the effect of an arbitrary cohesive force proportional to the particle buoyant weight, [38, 39] and segregation in fluidized beds of bidisperse particles. [40]

Even with the high speed computing available today, one can only simulate small systems, which are orders of magnitude smaller than real vibrated fluidized beds, through this hybrid approach. Therefore, it is essential that one choose suitable, idealized problems to probe the underlying mechanics. With this in mind, we have chosen essentially one-dimensional (1D) vibrated fluidized beds of particles, applying periodic boundary conditions in the two lateral directions. This limits the macroscopic dynamics to the vertical direction only, and one obtains one-dimensional traveling waves (1D-TW) instead of bubble-like voids observed in experiments and in fully three-dimensional flow simulations; nevertheless, such an idealized problem is, in our opinion, adequate to expose the manner in which the vibrating base plate interacts with the bed particles and how dense cohesive regions are broken down into smaller agglomerates.

The rest of the paper is organized as follows. The DEM-based hybrid model is described in Sec. II, and bubble formation, realized as 1D-TW in our geometry (narrow cross sectional areas), is presented in Sec. III A. The effect of cohesion and vibration on the fluidization is presented in Sec. III B, and the manner in which the vibration enhances the fluidization will be discussed in Sec. III C. The pressure drop in vibrated fluidized beds and the mechanism through which the vibration breaks up cohesive assemblies will be presented in Sec. III D and Sec. III E respectively, which are followed by the conclusions in Sec. IV.

II. METHOD: DEM-BASED HYBRID MODEL

Since its introduction by Cundall and Strack [33] nearly three decades ago, the DEM has been successfully used in modeling various particulate flow problems, including hopper flows, [41] shearing cells, [42] rotating drums, [43] and oscillated layers. [44, 45] Comprehensive description of this method can be found in the literature. [46, 47, 48] Below, we briefly describe the main idea of the DEM, and subsequently focus on how the volume-averaged gas phase hydrodynamics is coupled with the individual particle dynamics in our model.

A. Discrete element method

In the DEM simulation, particles are modeled as “soft” sphere (the deformation is accounted for by overlaps), whose trajectories are computed by integrating Newton’s equations of motion. When objects (particles or system boundaries) get into contact, the interaction is resolved by decomposing the interaction force into the normal and tangential directions relative to the displacement vector between the objects at contact, $\mathbf{F}_{cont} = (\mathbf{F}_n, \mathbf{F}_s)$, and the energy dissipation upon contact is characterized by the inelasticity and the surface friction. We use the so-called spring-dashpot model, with a Hookean spring. [33] The objects are allowed to overlap upon contact, and the contact force in the normal direction \mathbf{F}_n is determined by the amount of overlap Δ_n and the normal component of the relative velocity at contact v_n ,

$$\mathbf{F}_n = (k_n \Delta_n - \gamma_n v_n) \hat{\mathbf{n}}, \quad (1)$$

where k_n is the spring stiffness in the normal direction, γ_n is the damping coefficient, and $\hat{\mathbf{n}}$ is the unit vector in the normal direction at contact, pointing from the contact point toward the particle center. The damping coefficient γ_n is related to k_n by the normal coefficient of restitution e ($0 \leq e \leq 1$),

$$\frac{4k_n/m^*}{(\gamma_n/m^*)^2} = 1 + \left(\frac{\pi}{\log e} \right)^2, \quad (2)$$

where $1/m^* = 1/m_i + 1/m_j$, and i and j are indices of interacting particles or objects. In principle, the value of k_n is determined by Young’s modulus of the material under consideration. However, unless stated otherwise, we use a much smaller value for k_n , compared to the one computed based on the usual range of Young’s modulus. If the main results are not qualitatively different, it is favorable to use a smaller value of k_n , because the collision duration time in DEM scales with $k_n^{-1/2}$, which determines the integration time-step size required to accurately resolve the interaction during the contact. This is a well-known issue in DEM simulations. [46, 47] We varied k_n over three orders of magnitude and verified that the main results do not depend sensitively on the choice of k_n , even though actual contact force between the objects certainly depend on the value of k_n . For instance, the results for two k_n values differing by a factor of 10 will be presented in Figs. 7, 8, and 9.

The interaction in the tangential direction is modeled by a “spring and slider”, and the contact force is given by:

$$\mathbf{F}_s = -\text{sign}(v_s) \times \min(k_t \Delta_s, \mu |\mathbf{F}_n|) \hat{\mathbf{s}}, \quad (3)$$

where $v_s = \mathbf{v}_s \cdot \hat{\mathbf{s}}$ is the tangential component of the relative velocity at contact; $\mathbf{v}_s = \hat{\mathbf{n}} \times (\mathbf{v}_{ij} \times \hat{\mathbf{n}})$; $\hat{\mathbf{s}}$ is the unit vector in the tangent plane collinear with the component of the relative velocity at contact; k_t is the tangential spring stiffness that is related to k_n by the Poisson’s ratio of the material ν_P [$k_t = 2k_n(1 - \nu_P)/(2 - \nu_P)$]; and Δ_s

is the magnitude of tangential displacement from the initial contact. The magnitude of the total tangential force is limited by the Coulomb frictional force $\mu |\mathbf{F}_n|$, where μ is the coefficient of friction. More sophisticated and/or realistic interaction models, such as that of Walton and Braun’s [49] or a Hertzian spring-dashpot model, [50] may also be used. However, we choose a simple Hookean spring-dashpot and spring-slider model, as it has been shown to successfully reproduce many experimental observations, [41, 43, 45] and it is computationally more tractable than others.

Among different inter-particle forces, other than due to contact, we consider only cohesion arising from van der Waals force. In principle, the cohesion can depend on the particle characteristics, such as polarizability, particle size, and asperity. [51] However, we adopt a simple formula by Hamaker, as we aim to bring out the effect of cohesion on the fluidization behavior, rather than to validate different cohesion models. Particulate flows in industry often consist of particles with a wide range of sizes and shapes; however, we seek a better understanding of simple systems consisting of monodisperse spheres, which are well characterized by a small set of parameters. The cohesive van der Waals force between two spheres of radii r_i and r_j can be expressed as, [51]

$$\begin{aligned} \mathbf{F}_c &= -\frac{A}{3} \frac{2r_i r_j (s + r_i + r_j)}{[s(s + 2r_i + 2r_j)]^2} \times \\ &\quad \left[\frac{s(s + 2r_i + 2r_j)}{(s + r_i + r_j)^2 - (r_i - r_j)^2} - 1 \right]^2 \hat{\mathbf{n}} \\ &\approx -\frac{A}{12} \frac{r}{s^2} \hat{\mathbf{n}} \quad (\text{for } r = r_i = r_j \text{ and } s \ll r), \quad (4) \end{aligned}$$

where A is the Hamaker constant, and s is the inter-surface distance. As the original formula is a rapidly decreasing function of s , further simplification using the assumption of $s \ll r$ has been made. This model has a singularity at contact. In order to avoid this artifact, we introduce a widely accepted minimum cut-off value for the inter-surface distance of 0.4 nm ($\equiv \delta^*$), which corresponds to the inter-molecular center-to-center distance. [52] In what follows, the level of cohesion is represented by the cohesive Bond number Bo , which is defined as the ratio of the maximum cohesive force (at the minimum cut-off separation δ^*) to the particle weight. Other types of cohesion can be readily accounted for in DEM-based models. [39, 53, 54]

B. Coupling with gas phase hydrodynamics

The dynamics of individual particles is coupled with the volume-averaged gas phase hydrodynamics. [34] In this hybrid model, the equations of motion for individual particles have two additional terms (compared to traditional DEM modeling particles in vacuum) arising from

the presence of the gas phase:

$$m_p \frac{d\mathbf{v}_p}{dt} = m_p \mathbf{g}_{eff} + \mathbf{F}_{cont} + \mathbf{F}_c + \frac{V_p}{\phi} \beta(\phi) (\mathbf{u}_g - \mathbf{v}_p) - V_p \nabla p, \quad (5)$$

where m_p and \mathbf{v}_p are individual particle mass and velocity, respectively. The first term on the right hand side represents the body force due to gravity; \mathbf{g}_{eff} is the effective gravitational acceleration in the reference frame where equations are integrated. For non-vibrated beds, \mathbf{g}_{eff} is simply the gravitational acceleration \mathbf{g} . When the bed is subject to a single frequency oscillation, the equations are integrated in the vibrated frame, and $\mathbf{g}_{eff} = \mathbf{g}[1 + \Gamma \sin(2\pi ft)]$, where $\Gamma = A_p(2\pi f)^2/g$ is the maximum acceleration of the base plate (distributor) non-dimensionalized by the gravitational acceleration $g = |\mathbf{g}|$, A_p is the oscillation amplitude, and f is the oscillation frequency. We assume the oscillating base plate is made of the same materials as the particles (the same values for e and μ), and that the mass of the plate is infinitely large compared to that of an individual particle. The second term and the third term represent the aforementioned contact force and van der Waals force, respectively. The total force acting on the particles due to the fluid is commonly partitioned into the local drag part and the effective buoyant part, as was done here (see e.g., an article by Ye et al. [37]): The fourth term accounts for the drag force, and the last term accounts for the contribution of the gradually varying part of the pressure field, where V_p is the volume of each particle; ϕ and \mathbf{u}_g are volume-averaged solid phase volume fraction and gas phase velocity, respectively; β is the inter-phase momentum transfer coefficient [31]; and p is the gas phase pressure.

In general, the gas phase quantities are obtained by simultaneously integrating the coarse-grained mass and momentum balance equations. We assume the gas phase to be incompressible, which will be validated later (see Sec. III D). The addition of continuity equations for the gas phase and solid phase reads

$$\nabla \cdot [(1 - \phi)\mathbf{u}_g + \phi\mathbf{u}_s] = 0, \quad (6)$$

and a reduced momentum balance equation for the gas phase, based on generalized Darcy's law, is given as

$$0 = -(1 - \phi)\nabla p + \beta(\phi) (\mathbf{u}_s - \mathbf{u}_g), \quad (7)$$

where \mathbf{u}_s is the coarse-grained solid phase velocity. Coarse-grained variables are considered only on grids where the continuum balance equations are solved. Note that the solid phase continuum (or coarse-grained) variables are explicitly available in the course of DEM computation.

C. Beds of narrow cross sectional area

Only beds of narrow cross sectional areas will be considered, and the volume-averaged gas phase (hence the

solid phase coarse-grained variables as well) is assumed to be 1D. However, the solid phase is maintained to be 3D, as the way particles pack and collide in lower dimensions are considerably different from those in realistic 3D cases. Our assumption allows us to consider relatively deep beds (through inexpensive computational effort) and to bring out the basic physics of more complicated dynamics in higher dimensions.

Solid phase coarse-grained variables at 1D discrete grid points are computed by distributing the particle mass and momenta to the nearest two grid points using a halo function h that continuously decreases to zero around the particle;

$$h(z - z_0) = \begin{cases} 1 - |z - z_0|/\Delta z & \text{for } |z - z_0| < \Delta z, \\ 0 & \text{otherwise,} \end{cases} \quad (8)$$

where z is the particle position in the vertical direction, z_0 is that of a neighboring grid point, and Δz is the grid spacing. It is readily seen that h has the property that the particle quantities are distributed to the two nearby grid points, inversely proportional to the distance to the grid point. The coarse-grained variables, the number density n and \mathbf{u}_s , on the grids are then defined simply as

$$n(z_0) = \sum_{i=1}^N h(z_i - z_0), \quad (9)$$

$$n(z_0)\mathbf{u}_s(z_0) = \sum_{i=1}^N h(z_i - z_0)\mathbf{v}_{p,i}. \quad (10)$$

where z_i and z_0 are the i th particle location and nearby grid location, respectively.

The assumption of the gas phase to be 1D facilitates further mathematical simplifications of the above particle-gas interaction formulation. In 1D continuum cases, Eq. (6) can be integrated

$$(1 - \phi)\mathbf{u}_g + \phi\mathbf{u}_s = \mathbf{U}_s, \quad (11)$$

where \mathbf{U}_s is the superficial gas flow velocity. Strictly speaking, in a vibrated fluidized bed, \mathbf{U}_s may also vary periodically. The extent of its variation will depend on the dynamics of the gas in the plenum and the flow resistance offered by distributor (base plate). One can show that the temporal variation of \mathbf{U}_s will be small for a highly resistive distributor plate, which we assume. Thus, in modeling of both non-vibrated and vibrated fluidized beds, \mathbf{U}_s will be considered to be a time-independent parameter.

After some manipulation, Eq. (5) can be rewritten as follows:

$$m_p \frac{d\mathbf{v}_p}{dt} = m_p \mathbf{g}_{eff} + \mathbf{F}_{cont} + \mathbf{F}_c + \frac{V_p}{\phi} \beta(\phi) \times \left[(\mathbf{u}_s - \mathbf{v}_p) - \frac{1}{(1 - \phi)^2} (\mathbf{u}_s - \mathbf{U}_s) \right]. \quad (12)$$

Note that the presence of the gas phase is realized as additional terms involving coarse-grained variables, instead of separate continuum equations to be integrated

simultaneously. In the course of integration, ϕ and \mathbf{u}_s in Eq. (12) need to be evaluated at the particle location, not at the grid points. We evaluate them by linearly interpolating those values at the neighboring grid points.

For the inter-phase momentum transfer coefficient β , we use an expression proposed by Wen and Yu [55]:

$$\beta = \frac{3}{4} C_D \frac{\rho_g \phi (1 - \phi) |\mathbf{u}_g - \mathbf{u}_s|}{d_p} (1 - \phi)^{-2.65}, \quad (13)$$

where C_D is the drag coefficient, ρ_g is the gas phase mass density, and d_p is the particle diameter. The drag coefficient proposed by Rowe [56] is employed in our model:

$$C_D = \begin{cases} \frac{24}{Re_g} (1 + 0.15 Re_g^{0.687}), & Re_g < 1000, \\ 0.44, & Re_g \geq 1000, \end{cases} \quad (14)$$

where

$$Re_g = \frac{(1 - \phi) \rho_g d_p |\mathbf{u}_g - \mathbf{u}_s|}{\mu_g}, \quad (15)$$

and μ_g is the gas phase viscosity. As we consider fine powders, Re_g is generally small, and we use the assumption $Re_g \ll 1$, which further simplifies β :

$$\beta(\phi) = 18 \frac{\mu_g}{d_p^2} \phi (1 - \phi)^{-2.65}. \quad (16)$$

Casting Eqs. (12) and (16) in a dimensionless form, using ρ_s , d_p , $\sqrt{g d_p}$, $\sqrt{d_p/g}$ as characteristic density, length, velocity, and time, one obtains the following non-dimensional groups (arrows indicate changes in the notation from dimensional variables to non-dimensional variables that will be used henceforth):

$$\begin{aligned} k_n &\leftarrow \frac{k_n}{\rho_s g d_p^2}, && \text{spring stiffness} \\ U_s &\leftarrow \frac{U_s}{\sqrt{g d_p}}, && \text{superficial gas flow rate} \\ \delta &\equiv \frac{\delta^*}{d_p}, && \text{scaled minimum separation distance} \\ Bo &\equiv \frac{A}{4\pi \rho_s g d_p^2 \delta^{*2}}, && \text{cohesive Bond number} \\ St &\equiv \frac{\rho_s g^{1/2} d_p^{3/2}}{\mu_g}, && \text{Stokes number} \end{aligned}$$

together with non-dimensional parameters, namely Γ , $f \leftarrow f \sqrt{d_p/g}$, e , μ , and ν_P .

III. RESULTS AND DISCUSSION

We simulate both non-vibrated and vibrated gas-fluidized beds of non-cohesive or cohesive particles ($0 \leq Bo \leq 50$). We consider beds of narrow square-shaped cross sectional area $5d_p \times 5d_p$ or $10d_p \times 10d_p$ with static depth $H_0 \sim 100d_p$ and $H_0 \sim 200d_p$ (which consist of

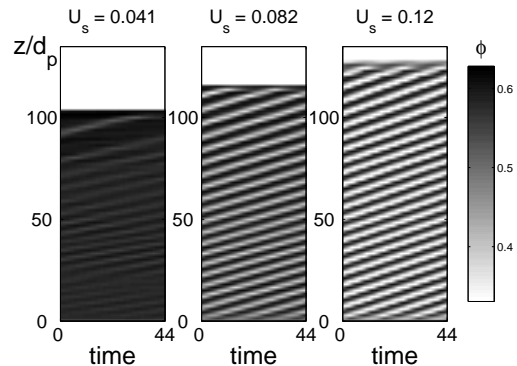


FIG. 1: Spatiotemporal plots of conventional fluidized beds of non-cohesive particles ($Bo = 0.0, St = 55$) at three different superficial gas flow rates. Gray scale represents the local volume fraction of particles; both the regions of the minimum value ($\phi \sim 0.33$) in the gray scale bar and completely void regions ($\phi = 0$) above the bed top surface are shown in the same white color.

3000 and 6000 particles respectively, in beds of $5d_p \times 5d_p$ cross section). Periodic boundary conditions are imposed in both lateral directions, in order to avoid strong side wall effects in beds of such a small aspect ratio. We check that our results do not sensitively depend on a particular choice of cross sectional area or the depth of the bed (e.g., see Fig. 2). We mostly use a bed of $\sim 5d_p \times 5d_p \times 100d_p$ in the following computations, unless otherwise stated. We used d_p , $1.5d_p$, and $2d_p$ for the grid spacing Δz . The detailed profiles of the coarse-grained variables slightly depend on the choice of Δz (the bigger the grid size is, the smoother the variables are, as one can readily expect), but the main results remain the same, unless the grid size is too large; we set $\Delta z = 1.5d_p$ in all the results presented here. In the following, all the quantities will be shown in non-dimensional form.

A. Bubbling and one-dimensional traveling waves

We start by considering conventional (non-vibrated) gas fluidized beds of non-cohesive particles to make certain that our model captures basic experimental observations. We first estimate the minimum fluidization velocity through a simulation of quasi-static increase in the gas flow rate (from zero) and the measurement of the pressure drop across the bed, which yields $U_{mf} \approx 0.022$. This estimate is slightly smaller than what we can compute using the force balance relation and the approximate formula of Wen and Yu, $U_{mf} \approx 0.023$ [57]; in this calculation, we used $\phi_{mf} = 0.652$, which is measured from the bulk of the bed. When the gas flow rate exceeds U_{mf} , the bed in our model starts to expand inhomogeneously, and forms alternating bands of plugs and voids. Particles located at the bottom of one plug “rain down” through a

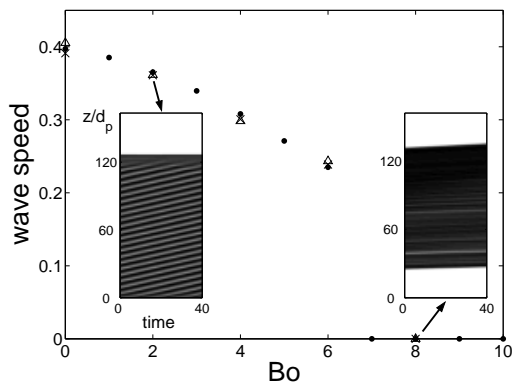


FIG. 2: Traveling wave speed (filled circles) in non-vibrated gas-fluidized beds ($\Gamma = 0$), for various levels of cohesion. $U_s = 0.12$. Beds of larger Bo 's ($> \sim 6$) do not get fluidized; rather the whole bed moves up as a plug. Insets are spatiotemporal plots of moderately cohesive bed that is fluidized ($Bo = 2$) and more cohesive bed ($Bo = 8$) that is not fluidized and rises as a plug at this flow rate. Triangles: The wave speeds obtained in beds of $\sim 5d_p \times 5d_p \times 200d_p$. Crosses: The wave speeds obtained in beds of $\sim 10d_p \times 10d_p \times 100d_p$.

void region and accumulate at the top of the lower plug, causing the void regions to rise to the top in a periodic fashion (Fig. 1). This phenomenon corresponds to the formation of a periodic train of bubble-like voids in real fluidized beds, which appears as 1D-TW in the narrow beds we consider. These waves represent the first stage in the bifurcation hierarchy leading to various inhomogeneous structures in higher-dimensional (i.e. 2D or 3D) fluidized beds. [58, 59, 60] The secondary bifurcations which occur in real fluidized beds are suppressed in our simulations, which are forced to retain the 1D character. As the gas flow rate increases, both the wave speed and amplitude increase (Fig. 1). In the subsequent Sections, we will use the 1D-TW as an indicator that characterizes the fluidizability of the bed.

B. Cohesion, vibration, and fluidization

When the gas flow rate is well above U_{mf} , the bed exhibits clearly visible 1D-TW [for instance, see the cases of $U_s = 0.082$ and 0.12 in Fig. 1]. In this Section, we examine the influence of the cohesion (between particles) on the fluidizability of a bed, and explore how mechanical vibration facilitates the fluidization of beds of cohesive particles.

Figure 2 shows the effect of Bo on the wave speed, where we have kept $St \sim 55$ and $U_s = 0.12$ (the same values as in the last panel of Fig. 1). As Bo increases, the wave gradually slows down, and eventually disappears. At $Bo = 6$, the wave travels intermittently, remaining stationary for some time and traveling at other times, and the wave speed during the non-stationary phase is

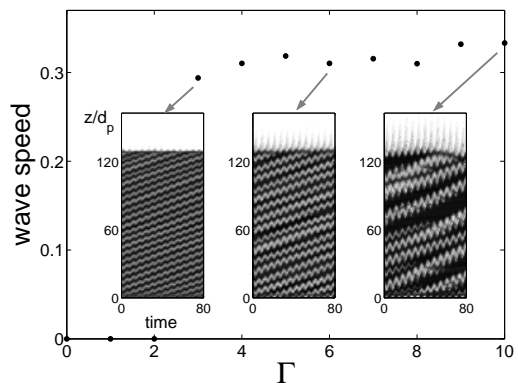


FIG. 3: Traveling wave speed in beds of highly cohesive powders ($Bo = 20$) subject to vibrations with various levels of Γ . The traveling wave reappears for $\Gamma > 2$. Insets are spatiotemporal plots of three different cases ($\Gamma = 3.0, 6.0, 10$), shown in the vibrating plate frame. $f = 0.16$; $U_s = 0.12$.

shown in Fig. 2. For $Bo > 7$, the whole bed rises up as a plug at this flow rate, which is consistent with the well-known experimental observations in narrow beds of strongly cohesive particles (see a review article by Sundaresan [60] and references therein). Further increase of U_s only slightly improves the fluidizability of the bed, confirming that beds of highly cohesive particles cannot be fluidized by simply increasing the gas velocity.

The results shown in Fig. 2 are obtained with the assumption that the interaction between the particle and the base plate is non-cohesive. We check that the adhesion at the base plate does not make any difference in the above results, as well as all the main results presented here. The only noticeable difference is that strongly cohesive particles at the bottom of a bed get stuck to the plate for some time (during a cycle; in vibrated beds), depending on the oscillation parameters and the superficial gas flow velocity. Detailed comparison between the two cases (with and without adhesion) is shown later in Fig. 7.

Now we subject beds of even more cohesive particles ($Bo = 20$) to mechanical vibration of a single frequency sinusoidal oscillation in the direction of gravity. When the vibration intensity is strong enough (when Γ exceeds a certain value), even these highly cohesive beds get fluidized in the sense that 1D-TW reappears (Fig. 3). At a fixed gas flow rate (we assume it to be time-independent; see the discussion in Sec. II C), the wavelength apparently increases with Γ ; however, the wave speed remains nearly the same (Fig. 3). We define the critical Bond number Bo_c as the maximum value of Bo for which the bed is fluidizable (generating 1D-TW) at given set of oscillation parameters, and compute it as functions of Γ and f , using bisection-type search along the Bo -axis. We find that Bo_c increases almost linearly with Γ (Fig. 4), but it only weakly depends on f (Fig. 5). The frequency range shown in this figure corresponds to the usual operation

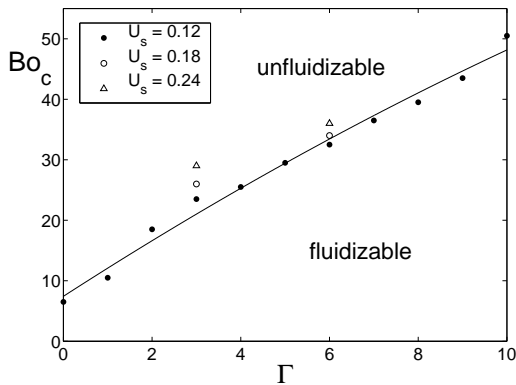


FIG. 4: The critical values of Bo_c , above which the bed does not get fluidized at given vibration parameters, as a function of Γ . Three different levels of U_s are used for $\Gamma = 3.0$ and 6.0 . $f = 0.16$. A solid line, the least square fit for the cases of $U_s = 0.12$, is included to guide the eye.

range between 10 Hz and 100 Hz, for the particle size of $d_p = 50 \mu\text{m}$. In this range of frequencies, Bo_c is virtually independent of the frequency. As the gas flow rate increases, Bo_c slightly increases at fixed values of Γ and f (see the cases for $\Gamma = 3$ and 6 in Fig. 4).

C. The role of vibration: Direct impact vs. pressure pulsation

In this Section, we discuss the manner in which the vibrating base plate or the distributor, interacts with the bed material.

In the absence of gas, the kinetic energy of individual particles in vibrated beds is obtained only from direct impact with the plate, and dissipated through interaction between particles. In shallow beds ($H_0 < \sim 20d_p$), the fluctuating kinetic energy (granular temperature) dissi-

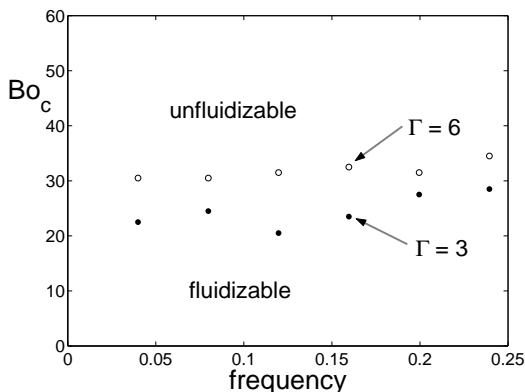


FIG. 5: The critical values of Bo_c as a function of f , for two different levels of Γ . $U_s = 0.12$.

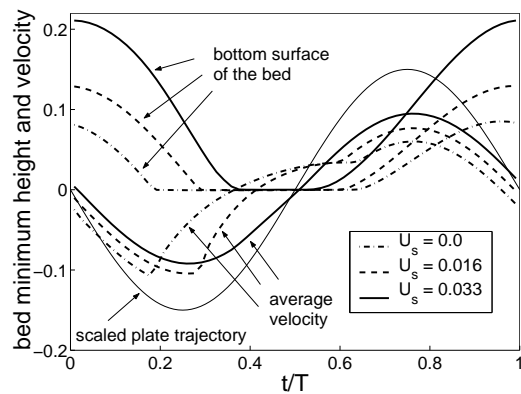


FIG. 6: The bottom surface and the average vertical velocity of vibrated beds (averaged over all the particles in the bed) during a cycle, shown in the *vibrating frame*, obtained for three different gas flow velocities. $Bo = 20$; $\Gamma = 3.0$; $f = 0.16$. A thin solid line, an arbitrarily rescaled plate trajectory in the laboratory frame, is drawn to represent the phase angle during a cycle.

pates so quickly through collisions that the whole bed can be well approximated by one solid body. The dynamics of the center of mass of such a bed can be described by that of single perfectly inelastic ball on a vibrating plate. [61] Vibrated shallow beds in vacuum undergo period doubling bifurcations as Γ is varied. [62] Such layers of a large aspect ratio form various spatiotemporal standing wave patterns. [17, 18] However, temporal dynamics of vibrated deep beds (of about 20 particle deep or more) in vacuum are not commensurate with the oscillation frequency, and exhibit more complicated non-periodic behavior. [63]

When the gas phase effects are accounted for, the gas drag causes the dynamics of vibrated deep beds to deviate from those in vacuum, and the deviation is more pronounced for smaller particles (because the gas drag is larger). For deep beds of fine powders considered here, the presence of gas phase modifies the bed dynamics so that the temporal dynamics become periodic. In the absence of a net flow ($U_s = 0$) the bed lifts off from the plate only slightly (even smaller than the particle size) during a fraction of a cycle, and the bed impacts the plate later in the same cycle (dot-dashed lines in Fig. 6). This periodic behavior has the same periodicity as the plate oscillation. Even for higher values of Γ , period doubling phenomenon, which occurs in vibrated shallow layers in vacuum, is not observed. Note that, in the early phase of the oscillation cycle shown in Fig. 6 ($0 < t/T < 0.25$), the plate moves downwards (and so does the base plate), and yet the bottom surface of the bed is approaching the distributor plate. i.e. the bed is descending faster than the plate. The bed hits the plate, stays in contact for a duration of time, and then detaches from it.

When the gas flow is turned on and its rate gets increased, the velocity of the bed (relative to the base plate)

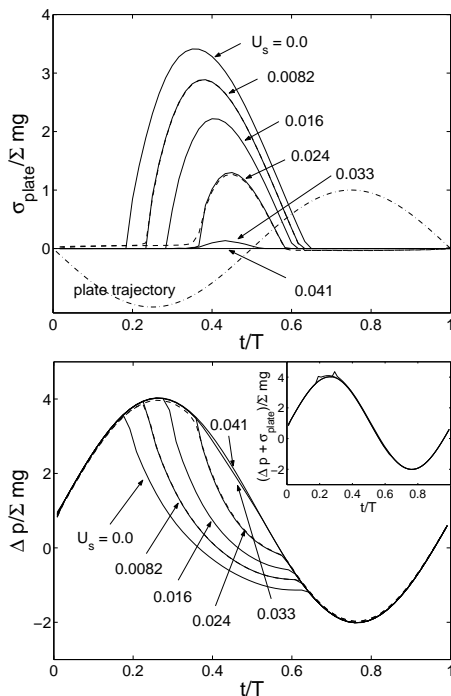


FIG. 7: (Top) Normal stress tensor on the base plate, scaled by the bed weight per unit cross sectional area (Σmg), is shown during a cycle for different superficial gas flow rates. $Bo = 20$; $\Gamma = 3.0$; $f = 0.16$; $k_n = 2.0 \times 10^5$. Solid lines are obtained by neglecting adhesion at the base plate (Bo_p , the Bo at the plate, is 0). Dashed lines are obtained when the adhesion is accounted for ($Bo_p = 40$), for two cases ($U_s = 0.0082, 0.024$), which are nearly the same as the non-adhesive cases. A dot-dashed line, the plate trajectory in an arbitrary unit, is drawn to represent the phase angle during a cycle. (Bottom) The scaled pressure drop for the same cases as in the top panel. Inset shows the sum of the pressure drop and the normal stress at the base plate for three cases ($U_s = 0.0, 0.016, 0.033$), all of which virtually coincide with the reduced effective gravity (g_{eff}/g) in the vibrating frame [sinusoidal curve; $1 + \Gamma \sin(2\pi ft)$]. Small excess amounts, appearing as small peaks on top of a sinusoidal curve, arise from the transient restoring force of the *soft* particles at the impact, which gradually disappears as the plate impacts the bed more gently with increasing U_s (there are no apparent additional peaks for $U_s = 0.033$).

during its short flight increases, and the bed lifts off further from the plate (Fig. 6). The upward gas flow resists downward motion of the bed, hence not only the duration of direct impact but also its magnitude (strength) gradually decreases (top panel in Fig. 7), as the gas flow rate increases. When the adhesion at the base plate is accounted for (dashed lines in Fig. 7), the plate experiences some force even when the bulk of the bed is in flight ($t/T < \sim 0.2$ or $> \sim 0.6$), as there are a small number of particles stuck to the plate. Other than this, compared to the case when the adhesion is neglected (solid lines), no difference is observed. The bed eventually hardly touches

the plate at some gas flow rate, above which direct impact remains minimal. It will be shown in the next Section that the minimum gas flow rate at which the direct impact virtually vanishes is for all practical purposes the same as the minimum fluidization velocity in vibrated beds.

D. Pressure drop in vibrated beds

The pressure drop across vibrated beds oscillates with the same periodicity as the plate oscillation (bottom panel in Fig. 7). The pressure drop increases (decreases) when the base plate moves down (up); see Fig. 6 and the bottom panel in Fig. 7, for $t/T < \sim 0.5$. At first glance, this seems to be counter-intuitive, as the pressure drop increases when the plate is “moving away”. However, it should be noted that the change in the pressure drop is determined by the change in the gap between the bed and the base plate (i.e. the relative motion with respect to the plate), not by the absolute motion of the base plate in the laboratory frame. As noted in the previous Section, the bed approaches the plate during the phase of the oscillation cycle when the plate is moving down from its mean position.

As soon as impact occurs, the pressure drop begins to decrease rapidly, even below zero. While the bed is moving away from the plate after the take-off (see $t/T > \sim 0.6$ in Fig. 6), the pressure drop continues to decrease. During this time, a region of lower pressure is being created in the gap between the bed and the plate (bottom panel in Fig. 7). Our results are generally consistent with the experimental measurements by Thomas *et al.* [64]; however, direct comparison with their data is not possible because of differences in systems and particle properties. As the gas flow rate increases, the abrupt drop at the impact gets smaller until it virtually vanishes (and so does a sudden increase in the stress at the plate σ_{plate}), and the pressure drop curve during a cycle approaches nearly the same, asymptotic sinusoidal curve.

When the vertical component of the stress at the plate is combined with the pressure drop for each case, the resulting curves for different gas flow rates virtually coincide with the same sinusoidal curve (inset in bottom panel of Fig. 7). This can be understood from the following force balance relation in the direction of gravity:

$$\frac{\sigma_{plate}}{\Sigma mg} + \frac{\Delta p}{\Sigma mg} = \frac{g_{eff}}{g}, \quad (17)$$

where Σmg is the weight of the bed per unit cross sectional area, and the restoring force due to the softness of the particles (i.e., the spring stiffness) is neglected. The above relation holds at every moment during a cycle, and the asymptotic common sinusoidal curve in the inset is identified to be $1 + \Gamma \sin(2\pi ft)$. It corresponds to the effective gravity in the vibrating plate frame g_{eff}/g , the right hand side of Eq. (17). Using the fact that the

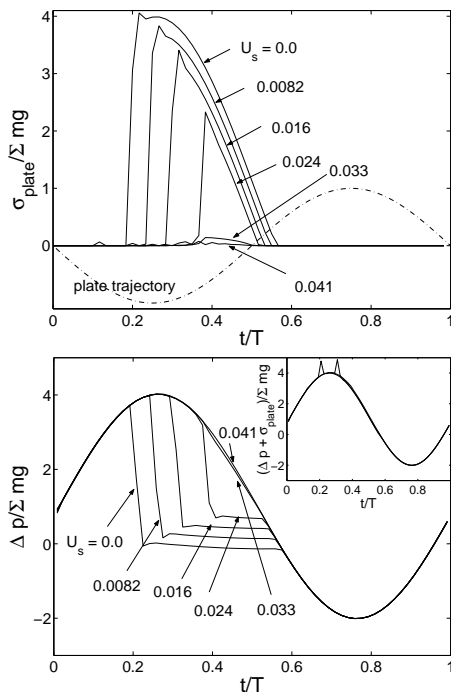


FIG. 8: The same quantities measured for the same cases as in Fig. 7 except that the spring stiffness k_n and k_s have been increased by a factor of 10 (e.g., $k_n = 2.0 \times 10^6$).

pressure drop across the bed is limited by $(1 + \Gamma) \sum mg$ during a cycle, we can examine the validity of the incompressibility assumption for the gas phase that we use: By making use of the equation of state for an ideal gas, one can show that the ratio of the change in gas phase density $\Delta\rho_g$ to its reference value ρ_{ref} satisfies $\Delta\rho_g/\rho_{ref} \approx \Delta p/P_{atm} \leq (1 + \Gamma) \sum mg/P_{atm}$, where P_{atm} is the atmospheric pressure. For the beds of fine powders considered in our study, $\sum mg/P_{atm} \sim \mathcal{O}(10^{-5})$, hence $\Delta\rho/\rho_{ref} \ll 1$ and the assumption of the incompressibility is valid at *every* moment during a cycle.

In order to test the sensitivity of the results to the spring stiffness, we repeated the calculations shown in Fig. 7 with an order of magnitude larger value of k_n . The results are presented in Fig. 8. The detailed behavior during a cycle surely depends on the value of the spring stiffness; the beds of softer particles in Fig. 7 noticeably further compress and expand during the impact, and the pressure drop keeps decreasing even below zero *during* the impact. This effect diminishes when a larger value is used for k_n ; in spite of the quantitative changes that are readily apparent, the results shown in Figs. 7 and 8 are qualitatively similar. Importantly, in a fully fluidized state, pressure pulsation is the only relevant mechanism in both cases, and the value of k_n becomes irrelevant.

Viewing the pressure pulsation at the bottom plate as a forcing set up by the plate, one can inquire about the speed at which this pulsation propagates upwards through the bed. As we have taken the gas phase to

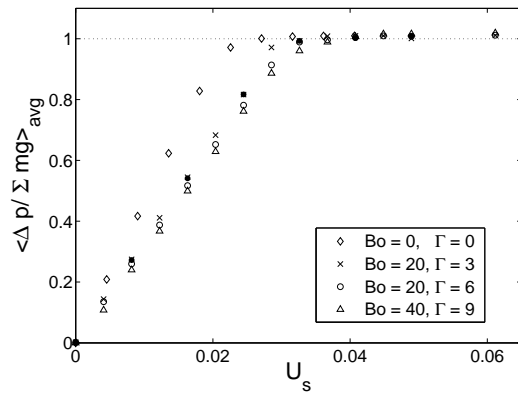


FIG. 9: The average pressure drop during a cycle, scaled by the bed weight per unit cross sectional area, obtained for different cases of vibrated fluidized beds, as a function of U_s . The pressure drop in conventional fluidized beds of non-cohesive particles (diamonds) is included for comparison. Filled circles are for the case of $Bo = 20$, $\Gamma = 3.0$, but 10 times larger value of spring stiffness ($k_n = 2.0 \times 10^6$), compared to all the other cases ($k_n = 2.0 \times 10^5$), was used.

be incompressible, the pulse propagates nearly instantaneously. Thus, at each time instant, the gas pressure decreases essentially monotonically as one moves up through the bed (except for the small periodic variation associated with the voidage waves). If one allows the gas to be compressible, then the pulsation travels at the speed of sound; sound speed through gas-fluidized beds is considerably smaller than that through a column of gas. [65] If the time required for the propagation of the pulsation through the bed is commensurate with the period of the plate oscillation, resonance can set in; however, such resonance is suppressed in the present study as we have treated the gas as incompressible. In any case, in the relatively shallow beds that we consider, resonance is not expected to be a significant effect.

The pressure drop averaged throughout a cycle as a function of gas flow rate manifests a linear increase up to the constant plateau region (Fig. 9), which is qualitatively the same as in conventional fluidized beds. The minimum velocity when the direct impact virtually does not occur is essentially the same as the minimum fluidization velocity in vibrated beds; only the pressure pulsation is a relevant mechanism for a fluidized state of vibrated beds. Note that the minimum fluidization velocities for the vibrated beds of cohesive particles are larger than that for a non-vibrated bed of non-cohesive particles of the same size. This can be interpreted as the increment in effective particle size, which is understandable, because the fluidized entities in vibrated beds of cohesive particles are agglomerates, not individual particles. The average volume fraction at the minimum fluidization is smaller (e.g. $\phi_{mf} = 0.631$ for the case of $Bo = 40$), compared to what is observed in a bed of non-cohesive particles (0.652); cohesive beds tend to pack more loosely. In the

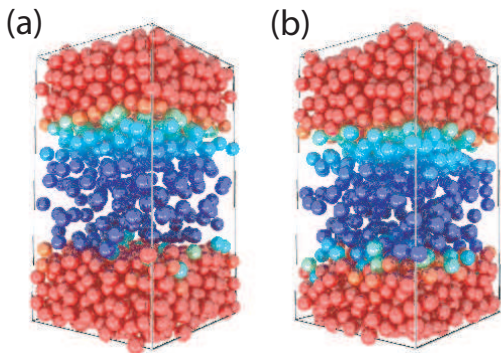


FIG. 10: [Color online: Particles are color-coded according to the vertical velocity, increasing from blue (moving downwards) to green to red (moving upwards)] Snapshots of beds of (a) non-cohesive particles ($Bo = 0$) and (b) cohesive particles ($Bo = 4$), obtained from particles in a box of height $L = 18d_p$ and cross sectional area $10d_p \times 10d_p$ ($\phi_{avg} = 0.40$). Periodic boundary conditions are imposed in all three directions (see text). Particles rain down from the upper plug to the lower plug, while void regions in the middle rise up, which form traveling voidage waves. Note that cohesive particles form strings or agglomerates while they rain down. Full animations are available from http://multiphase.princeton.edu/ICE_2005.

fully fluidized state, the pressure drop exhibits a plateau, which approximately equals the weight of the bed per unit cross sectional area (Fig. 9), as in non-vibrated beds. There is no clear consensus on this issue in experimental studies. Tasirin and Anuar [29] found that the pressure drop increases as the vibration intensity Γ increases, Erdész and Mujumdar [28] observed the opposite trend, and Marring et al. [7], Mawatari et al. [9], and Nam et al. [11] observed constant plateau pressure drop equaled with the bed weight per unit cross sectional area in high gas flow rates. Only the latter is consistent with our results, which can be explained by the simple force balance argument in Eq. (17), accounting for the fact that the direct impact is negligibly small in a fluidized state.

E. Break-up of cohesive assembly by pressure pulsation

We seek to understand how vibration facilitates the break-up of cohesive assemblies into agglomerates and maintains the propagation of the wave in a fluidized state. We analyze the profile of continuum variables, including the granular temperature T and the solid phase stress tensor σ (or the solid phase pressure), across the traveling wave during a cycle. As the waves in a bed of finite depth that we have considered thus far are not perfectly periodic, we consider an alternate, idealized geometry, where a wave is fully developed in a small periodic box (in all of three directions) of height L that is commensurate with the wavelength obtained in the vibrated fluidized

bed simulations described above. Note that the direct impact does not play an important role for a fully fluidized bed (Sec. III C; only the pressure pulsation does), and the vibrating plate does not have to be considered in such a case. For a fully fluidized state, the weight of the bed per unit cross sectional area is supported by the pressure drop:

$$p|_{z=0} - p|_{z=L} = \rho_p g_{eff} \phi_{avg} L, \quad (18)$$

where ϕ_{avg} is the average volume fraction.

Comparison between fully fluidized states of cohesive beds and non-cohesive beds on microscopic level reveals that cohesive particles form strings of particles or agglomerates while they rain down through void regions, whereas non-cohesive particles come down individually (Fig. 10; full animations are available from http://multiphase.princeton.edu/ICE_2005). As one can readily see, this effect arises from the attractive force between cohesive particles, which can be well characterized by tensile stress on a continuum level. We compute the stress tensor, consisting of a kinetic or dynamic part and a virial or static part, using the following microscopic relation [66]:

$$\sigma = \frac{1}{V} \left[\sum_i m_i \tilde{\mathbf{v}}_i \otimes \tilde{\mathbf{v}}_i - \sum_{c \in V} \mathbf{f}_c \otimes \mathbf{l}_c \right], \quad (19)$$

where $\tilde{\mathbf{v}}_i = \mathbf{v}_i - \langle \mathbf{v}_i \rangle$ is the fluctuating velocity of the i th particle, \otimes is the dyadic tensor product, \mathbf{f}_c is the interacting force between contacting particles 1 and 2, and $\mathbf{l}_c = \mathbf{r}_1 - \mathbf{r}_2$ is the displacement vector between the centers of particles under consideration. The second term is summed over all the contacts in the averaging volume V .

Now we consider the continuum level interpretation of vibrated fluidized beds of highly cohesive particles in a fully periodic box during an oscillation cycle (Fig. 11). During a cycle, the wave oscillates up and down with a net upward motion, as can be seen in cases of Fig. 3. We compute the solid phase continuum variables including the pressure, the trace of the stress tensor per dimension $\text{Tr}(\sigma)/D$. We compute them in the co-traveling frame (with the wave's net motion), averaged over 100 cycles for the purpose of variance reduction. While the pressure pulsation cyclically varies during a cycle, so do both the granular temperature and the stress tensor.

Figure 11 shows the variation of solid phase continuum variables at six different times during an oscillation cycle. The inset in each panel shows the position of a hypothetical, oscillating base plate at the instant the profiles of the continuum variables are shown. The plate trajectory sketched in the insets can be compared to that shown in the top panel of Fig. 7. The corresponding pressure drop across the periodic domain can be found from the cyclically varying pressure drop profile in the bottom panel of Fig. 7, which is nearly out of phase with the plate position. In Fig. 11 (a), g_{eff}/g and the scaled pressure drop are nearly unity; they are larger in Fig. 11 (b); attain

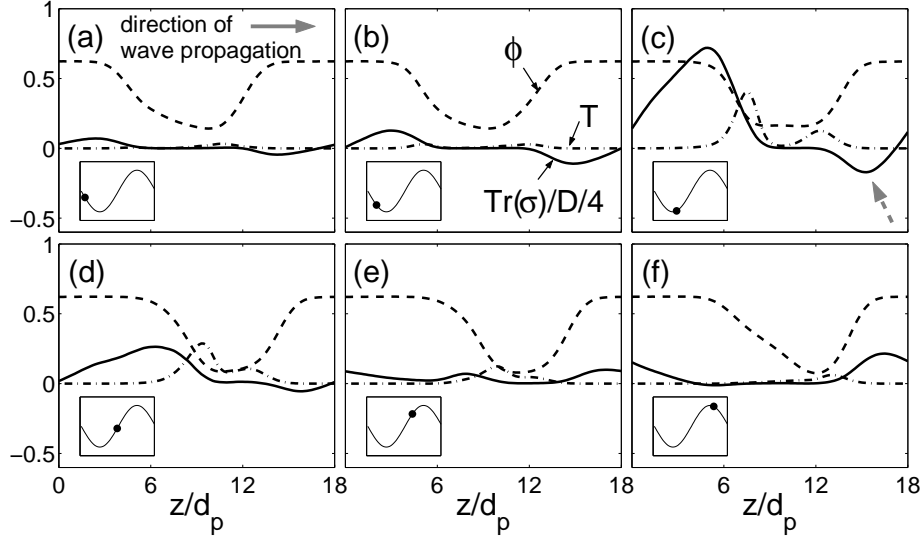


FIG. 11: Solid phase continuum variables of a highly cohesive bed ($Bo = 20, \phi_{avg} = 0.40$) during a cycle in the vibrating frame ($\Gamma = 3.0$), obtained in the same geometry as in Fig. 10. Insets represent the phase angle during a cycle in terms of the vertical location of the (virtually existing) base plate (indicated by dots). The void region in the middle oscillates up and down, and has an upward net motion [indicated by a gray arrow in panel (a)]. The solid phase stress during a cycle can be summarized by the following stages: (a) The pressure pulsation is weak and the particle phase pressure is negligibly small throughout the bed. (b) As the pressure pulsation increases, so do the magnitude of the normal stress both in compressive (in lower plug) and tensile regions (in upper plug) and granular temperature, (c) until they reach their maximum values; around this time the tensile stress reaches the tensile strength of the material, which breaks up the cohesive assembly into agglomerates. (d) Then the stress relaxes. (e) and (f) Relatively small compressive stress builds up at the bottom of the upper plug, but this is not relevant for the break-up of the assembly. The location of the peak tensile stress is indicated by a broken arrow in panel (c). A full animation during two cycles is available from http://multiphase.princeton.edu/ICE_2005.

their largest values near the instant shown in Fig. 11 (c); relax back towards unity in Fig. 11 (d); and then they decrease in Fig. 11 (e) until they reach the minimum values in Fig. 11 (f).

When the scaled pressure drop is nearly unity [Fig. 11 (a)], the solid phase pressure is negligibly small throughout the bed. As the pressure drop increases until it reaches its maximum value [Figs. 11 (b) and (c)], the granular temperature and compressive stress in the lower plug and tensile stress in the upper plug also increase significantly until they reach their maximum magnitudes. The large granular temperature occurs at the lower plug, where the particles or agglomerates get accumulated. It arises from vigorous collisions among raining down particles or agglomerates and the lower plug. Note that the volume fraction in this region is still low ($\phi < \sim 0.3$). A rough estimate for the magnitude of the stress using the values at the maximum temperature region ($\sim nT = 6/(\pi d_p^3)\phi T \sim 0.2$), where the most vigorous collisions occur, shows that it is still far smaller than the tensile strength of the cohesive assembly (~ 1) that is estimated below; here n is the number density. In order for these vigorous collisions to contribute to the break-up of the cohesive assembly, the magnitude of the stress formed by the collisions has to be comparable or larger than the tensile strength of the material. However, the stresses

formed by the collisions are not strong enough to break up the assembly, and irrelevant for the assembly break-up. Rather, it is the increased tensile stress in the upper plug that breaks up the assembly into agglomerates and maintains the wave propagation. Particles in the upper plug can split off from the assembly and rain down, because the increased tensile stress becomes large enough to reach the tensile strength of the cohesive assembly. It occurs at a time around that shown in Fig. 11 (c).

As the magnitude of the tensile stress cannot exceed the strength of the assembly, we estimate the strength of the fluidized bed by measuring the maximum tensile stress. We compare such obtained tensile strength of the fluidized bed with the prediction of Rumpf's model, [67]

$$\sigma_t = \frac{1 - \epsilon}{\pi} k \frac{F_t}{d_p}, \quad (20)$$

where σ_t is the tensile strength, ϵ is the porosity ($= 1 - \phi$), k is the coordination number, and F_t is the cohesive contact force. We find that our measurement ($\sigma_t \sim 0.8$) is about an order of magnitude smaller than the prediction ($\sigma_t \sim 6$). This discrepancy is understandable, because the cohesive assembly in a fluidized bed breaks up through the weakest linkage, as opposed to all directions as is assumed in the Rumpf's model.

Later in the cycle, when pressure drop decreases and approaches the minimum value [Figs. 11 (d) through (f)], the particle phase pressure is generally small in the bed. When the pressure drop is negative, relatively small compressive stress builds up at the bottom of the upper plug as the gas in the void region pushes up; this is obviously irrelevant for the break-up.

IV. SUMMARY

We have used a particle dynamics-based model for vibrated gas-fluidized beds of fine powders to study how the vibration facilitates the fluidization of beds of cohesive powders. We have demonstrated that, as the gas flow rate increases, the direct impact from the plate decreases and the pressure pulsation becomes more dominant. In a fluidized state, the latter is shown to be virtually the only relevant mechanism, and the pressure drop follows a simple sinusoidal curve during a cycle (Figs. 7 and 8), which corresponds to the weight of the bed per unit cross sectional area in the vibrated frame. As a consequence, the pressure drop averaged over a cycle in the fluidized state is simply the offset of this sinusoidal curve, which equals the weight of the bed per unit cross sectional area, as in non-vibrated beds. This relation can be readily understood by a simple force balance argument [Eq. (17)]. In a bubbling bed (which appears as 1D-TW in our study), it is during the transient time interval with large enough pressure pulsation when the increased tensile stress breaks up cohesive assembly into agglomerates (Fig. 11).

Note that the compressibility of the gas phase was ignored in the present study; it would be interesting to investigate resonance effects which may arise in vibrated beds by allowing for gas compressibility. It was also assumed that the gas superficial velocity is independent of time throughout the oscillation cycle, and this corresponds to the limit of very large resistance for gas flow through the distributor; it would also be interesting to examine the case of finite distributor resistance, where the superficial gas velocity can be expected to vary cyclically with plate vibration.

While the present study has yielded physical understanding of the pressure fluctuations induced by the plate and the tensile stress in the particle assembly, an analytical relation between vibration parameters and the agglomerate size is still elusive. Furthermore, we have considered only beds of narrow cross sectional areas, and assumed the volume-averaged gas phase to be 1D. Consequently, some generic behavior in real vibrated gas fluidized beds, such as horizontal sloshing motion of the particles, meandering gas flows around agglomerates, and more complicated bubble dynamics, were not allowed to occur. By avoiding such complexity, we were able to bring out certain basic physics of the bed dynamics. Future studies should investigate the dynamics of higher dimensional beds; however, simulation of fluidized beds

of realistic industrial scales, using the current approach, is not yet feasible.

Acknowledgment

This work was funded by The New Jersey Commission on Science and Technology, The Merck & Co., Inc., and an NSF/ITR grant. We are delighted to contribute this article to the special issue honoring WBR. Having him as a colleague and a friend has been a pleasure and a privilege for both SS and IGK. We salute his accomplishments and look forward to many more years of work and fun together.

Nomenclatures

A	= Hamaker constant
Bo	= cohesive Bond number between particles
Bo_p	= cohesive Bond number between particles and base plate
C_D	= drag coefficient
Δp	= pressure drop across the bed
Δz	= grid spacing for coarse-grained variables
d_p	= particle diameter
e	= normal coefficient of restitution
f	= vibration frequency
\mathbf{F}_{cont}	= interaction force due to contact
\mathbf{F}_c	= cohesive force due to van der Waals force
g_{eff}	= effective gravitational acceleration
h	= halo function
k	= coordination number
k_n	= spring stiffness in the normal direction
k_t	= spring stiffness in the tangential direction
m_p	= mass of individual particle
n	= solid phase number density
P_{atm}	= atmospheric pressure
p	= gas phase pressure
Re_g	= Reynolds number based on particle size
r	= particle radius
s	= inter-surface distance
St	= Stokes number
T	= granular temperature
Σmg	= bed weight per unit cross sectional area
\mathbf{u}_g	= volume-averaged gas phase velocity
\mathbf{u}_s	= volume-averaged solid phase velocity
U_s	= superficial gas flow velocity
U_{mf}	= minimum fluidization velocity
v_n	= relative velocity in normal direction
v_s	= relative velocity in tangential direction
\mathbf{v}_p	= velocity of individual particle
V_p	= volume of individual particle

Greek symbols

β	= inter-phase momentum transfer
δ, δ^*	= minimum separation distance for cohesion
Δ_s	= tangential displacement from initial contact
Δ_n	= amount of overlap in the normal direction
ϵ	= porosity (gas phase volume fraction)
ϕ	= solid phase volume fraction
γ_n	= damping coefficient for dashpot
Γ	= vibration intensity
μ	= coefficient of friction
μ_g	= gas phase viscosity
ν_P	= Poisson's ratio
ρ_g	= gas phase mass density
ρ_s	= solid phase mass density
σ	= solid phase stress tensor
σ_t	= tensile strength of the material
σ_{plate}	= vertical stress on the plate

TABLE I: Parameter values used.

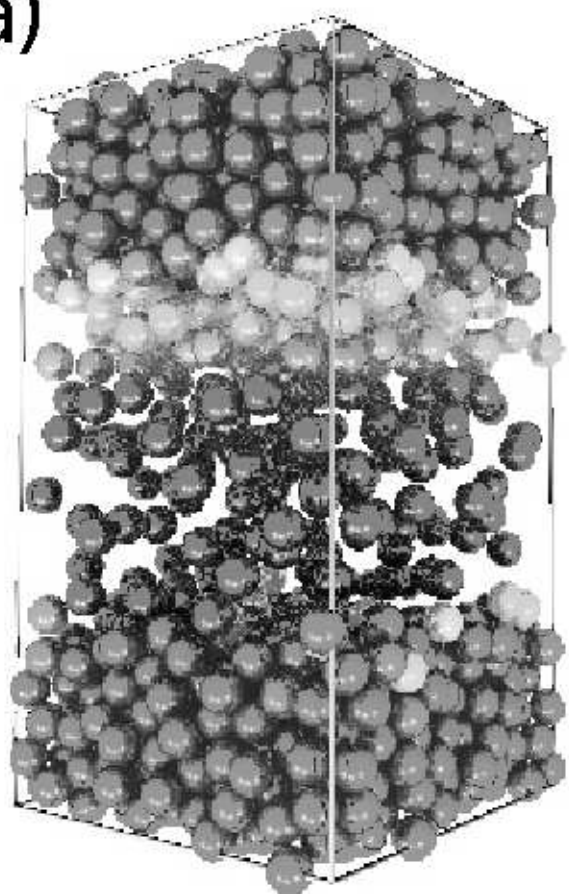
	Typical values for dimensional quantities	Nominal values for dimensionless parameters
μ_g	1.8×10^{-4} g/(m·s)	
g	981 cm/s ²	
d_p	50 μ m	
ρ_s	0.90 g/cm ³	
$\sqrt{gd_p}$	2.2 cm/s	
$\sqrt{d_p/g}$	2.3×10^{-3} s	
δ	0.4 nm (= δ^*)	8.0×10^{-6}
Δt	5.6×10^{-7} s	2.5×10^{-4}
$\Delta z/d_p$		1.5
e		0.9
μ		0.1
k_n		2.0×10^5 - 2.0×10^6
ν_P		0.3
Γ		0 - 10
f	$< \sim 100$ Hz	0 - 0.25

-
- [1] Geldart, D. Types of gas fluidization. *Powder Technol.* **1973**, 7, 285-292.
- [2] Visser, J. An Invited Review: Van der Waals and Other Cohesive Forces Affecting Powder Fluidization. *Powder Technol.* **1989**, 58, 1-10.
- [3] Mohan, M. R.; Dave, R. N.; Pfeffer, R. Promotion of deactivated sintering by dry-particle coating. *AIChE J.* **2004**, 49 (3), 604-618.
- [4] Ferguson, J. D.; Weimer, A. W.; George, S. M. Atomic layer deposition of ultrathin and conformal Al₂O₃ films on BN particles. *Thin Solid Films* **2000**, 371, 95-104.
- [5] Dutta, A.; Dullea, L. V. Effects of External Vibration and the Addition of Fibers on the Fluidization of a Fine Powder. *AIChE Symp. Ser.* **1991**, 87, 38.
- [6] Jaraiz, E.; Kimura, S.; Levenspiel, O. Vibrating beds of fine particles: estimation of interparticle forces from expansion and pressure drop experiments. *Powder Technol.* **1992**, 72, 23-30.
- [7] Marring, E.; Hoffmann, A. C.; Janssen, L. P. B. M. The effect of vibration on the fluidization behavior of some cohesive powders. *Powder Technol.* **1994**, 79, 1-10.
- [8] Wank, J. R.; George, S. M.; Weimer, A. W. Vibrofluidization of fine boron nitride powder at low pressure. *Powder Technol.* **2001**, 121, 195-203.
- [9] Mawatari, Y.; Koide, T.; Tatemoto, Y.; Uchida, S.; Noda, K. Effect of particle diameter on fluidization under vibration. *Powder Technol.* **2002**, 123, 69-74.
- [10] Mawatari, Y.; Tatemoto, Y.; Noda, N. Prediction of minimum fluidization velocity for vibrated fluidized bed. *Powder Technol.* **2003**, 131, 66-70.

- [11] Nam, C. H.; Pfeffer, R.; Dave, R. N.; Sundaresan, S. Aerated Vibrofluidization of Silica Nanoparticles. *AIChE J.* **2004**, *50*, 1776-1785.
- [12] Valverde, J. M.; Castellanos, A.; Quintanilla, M. A. S. Effect of vibration on the stability of a gas-fluidized bed of fine powder. *Phys. Rev. E* **2001**, *64*, 021302/1-8.
- [13] Chirone, R.; Massimilla, L.; Russo, S. Bubble-free fluidization of a cohesive powder in an acoustic field. *Chem. Eng. Sci.* **1993**, *48*, 41-52.
- [14] Nowak, W.; Hasatani, M. Fluidization and heat transfer of fine particles in an acoustic field. *AIChE Symp. Ser.* **1993**, *89*, 137.
- [15] Russo, P.; Chirone, R.; Massimilla, L.; Russo, S. The influence of the frequency of acoustic waves on sound-assisted fluidization of fine particles. *Powder Technol.* **1995**, *82*, 219-230.
- [16] Yu, Q.; Dave, R. N.; Zhu, C.; Quevedo, J. A.; Pfeffer, R. Enhanced fluidization of nanoparticles in an oscillating magnetic field. *AIChE J.* **2005**, *51*(7), 1971-1979.
- [17] Melo, F.; Umbanhowar, P. B.; Swinney, H. L. Transition to parametric wave patterns in a vertically oscillated granular layer. *Phys. Rev. Lett.* **1994**, *72*, 172-175.
- [18] Umbanhowar, P. B.; Melo, F.; Swinney, H. L. Localized excitations in a vertically vibrated granular layer. *Nature* **1996**, *382*, 793-796.
- [19] Möbius, M. E.; Lauderdale, B. E.; Nagel, S. R.; Jaeger, H. M. Brazil-nut effect: Size separation of granular particles. *Nature* **2001**, *414*, 270
- [20] Burtally, N.; King, P. J.; Swift, M. R. Spontaneous Air-Driven Separation in Vertically Vibrated Fine Granular Mixtures. *Science* **2002**, *295*, 1877-1879.
- [21] Moon, S. J.; Goldman, D. I.; Swift, J. B.; Swinney, H. L. Kink-induced transport and segregation in oscillated granular layers. *Phys. Rev. Lett.* **2003**, *91*, 134301/1-4.
- [22] Hong, D. C.; Quinn, P. V.; Luding, S. Reverse Brazil Nut Problem: Competition between Percolation and Condensation. *Phys. Rev. Lett.* **2001**, *86*, 3423-3426.
- [23] Naylor, M. A.; Swift, M. R.; King, P. J. Air-driven Brazil nut effect. *Phys. Rev. E* **2003**, *68*, 012301/1-4.
- [24] Möbius, M. E.; Cheng, X.; Eshuis, P.; Karczmar, G. S.; Nagel, S. R.; Jaeger, H. M. Effect of air on granular size separation in a vibrated granular bed. *Phys. Rev. E* **2005**, *72*, 011304/1-13.
- [25] Squires, A. M. Chemical process opportunities for vibrated powders: 2. In the field. *Powder Technol.*, **2004**, *147*, 10-19.
- [26] Musters, S. M. P.; Rietema, K. The effect of interparticle forces on the expansion of a homogeneous gas-fluidized bed. *Powder Tech.* **1977**, *18*, 239-248.
- [27] Liss, B. Incipient defluidization of sinterable solids. in *Fluidization*, pp. 249-256, AIChE, New York, 1983.
- [28] Erdész, K.; Mujumdar, A. S. Hydrodynamic Aspects of Conventional and Vibrofluidized Beds — A Comparative Evaluation. *Powder Technol.* **1986**, *46*, 167-172.
- [29] Tasirin, S. M.; Anuar, N. Fluidization Behavior of Vibrated and Aerated Beds of Starch Powders. *J. Chem. Eng. Jpn.* **2001**, *34*, 1251-1258.
- [30] Fan, L. S.; Zhu, C. *Principles of Gas-Solid Flows*, Cambridge University Press, Cambridge, 1998.
- [31] Gidaspow, D. *Multiphase Flow and Fluidization: Continuum and Kinetic Theory Description*, Academic Press, Boston, 1994.
- [32] Jackson, R. *The Dynamics of Fluidized Particles*, Cambridge University Press, Cambridge, 2000.
- [33] Cundall, P. A.; Strack, O. D. L. A discrete numerical model for granular assemblies. *Geotechnique* **1979**, *29*, 47-65.
- [34] Tsuji, Y.; Kawaguchi, T.; Tanaka, T. Discrete particle simulation of two-dimensional fluidized bed. *Powder Technol.* **1993**, *77*, 79-87.
- [35] Hoomans, B. P. B.; Kuipers, J. A. M.; Briels, W. J.; van Swaaij, W. P. M. Discrete particle simulation of bubble and slug formation in a two-dimensional gas-fluidized bed: A hard-sphere approach. *Chem. Eng. Sci.* **1996**, *51*, 99-118.
- [36] Xu, B. H.; Yu, A. B. Numerical simulation of the gas-particle flow in a fluidized bed by combining discrete particle method with computational fluid dynamics. *Chem. Eng. Sci.* **1997**, *52*, 2785-2809.
- [37] Ye, M.; van der Hoef, M. A.; Kuipers, J. A. M. A numerical study of fluidization behavior of Geldart A particles using a discrete particle simulation. *Powder Technol.* **2004**, *139*, 129-139.
- [38] Rhodes, M. J.; Wang, X. S.; Nguyen, M.; Stewart, P.; Liffman, K. Use of discrete element method simulation in studying fluidization characteristics: Influence of interparticle force. *Chem. Eng. Sci.* **2001**, *56*, 69-76.
- [39] Rhodes, M. J.; Wang, X. S.; Nguyen, M.; Stewart, P.; Liffman, K. Onset of cohesive behaviour in gas fluidized beds: a numerical study using DEM simulation. *Chem. Eng. Sci.* **2001**, *56*, 4433-4438.
- [40] Bokkers, G. A.; van Sint Annaland, M.; Kuipers, J. A. M. Mixing and segregation in a bidisperse gassolid fluidised bed: A numerical and experimental study. *Powder Technol.* **2004**, *140*, 176-186.
- [41] Zhu, H. P.; Yu, A. B. Steady-state granular flow in a three-dimensional cylindrical hopper with flat bottom: microscopic analysis. *J. Phys. D: Appl. Phys.* **2004**, *37*, 1497-1508.
- [42] Volfson, D.; Tsimring, L. S.; Aranson, I. S. Partially fluidized shear granular flows: Continuum theory and molecular dynamics simulations. *Phys. Rev. E* **2003**, *68*, 021301/1-15.
- [43] McCarthy, J. J.; Shinbrot, T.; Metcalfe, G.; Wolf, D. E.; Ottino, J. M. Mixing of granular materials in slowly rotated containers. *AIChE J.* **1996**, *42*, 3351-3363.
- [44] Mehta, A.; Barker, G. C. Vibrated powders: A microscopic approach. *Phys. Rev. Lett.* **1991**, *67*, 394-397.
- [45] Wassgren, C. R. Vibration of granular materials. Ph. D. dissertation, California Institute of Technology, 1997.
- [46] Herrmann, H. J.; Luding, S. Review Article: Modeling granular media with the computer. *Continuum Mech. Thermodyn.* **1998**, *10*, 189-231.
- [47] Duran, J. *Sands, Powders, and Grains: An Introduction To the Physics of Granular Materials*, Springer Verlag, New York, 2000.
- [48] Rapaport, D. C. *The Art of Molecular Dynamics Simulation*, Cambridge University Press, Cambridge, 2004.
- [49] Walton, O. R.; Braun, R. L. Viscosity, granular temperature, and stress calculations for shearing assemblies of inelastic, frictional disks. *J. of Rheology* **1986**, *30*, 949-980.
- [50] Schäfer, J.; Dippel, S.; Wolf, D. E. Force Schemes in Simulations of Granular Materials. *J. Phys. I* **1996**, *6*, 5-15.
- [51] Israelachvili, J. N. *Intermolecular and surface forces*, Academic Press, London, 1997.
- [52] Seville, J. P. K.; Willett, C. D.; Knight, P. C. Interpar-

- title forces in fluidization: A review. *Powder Technol.* **2000**, 113, 261-268.
- [53] Kuwagi, K.; Horio, M. A numerical study on agglomerate formation in a fluidized bed of fine cohesive particles. *Chem. Eng. Sci.* **2002**, 57, 4737-3744.
- [54] Mikami, T.; Kamiya, H.; Horio, M. Numerical simulation of cohesive powder behavior in a fluidized bed. *Chem. Eng. Sci.* **1998**, 53, 1927-1940.
- [55] Wen, C. Y.; Yu, Y. H. Mechanics of fluidization. *Chem. Eng. Prog. Symp. Ser.* **1966**, 62, 100-111.
- [56] Rowe, P. N. Drag forces in a hydraulic model of a fluidized bed: II. *Trans. Inst. Chem. Eng.* **1961**, 39, 175-180.
- [57] Davidson, J. F.; Clift, R.; Harrison, D. (Editors), *Fluidization*, 2nd Ed., Academic Press, London, 1985.
- [58] Glasser, B. J.; Kevrekidis, I. G.; Sundaresan, S. One- and two-dimensional traveling wave solutions in gas-fluidized beds. *J. Fluid Mech.* **1996**, 306, 183-221.
- [59] Glasser, B. J.; Sundaresan, S.; Kevrekidis, I. G. From Bubbles to Clusters in Fluidized Beds. *Phys. Rev. Lett.* **1998**, 81, 1849-1852.
- [60] Sundaresan, S. Instabilities in fluidized beds. *Annu. Rev. Fluid Mech.* **2003**, 35, 63-88.
- [61] Mehta, A.; Luck, J. M. Novel temporal behavior of a nonlinear dynamical system: The completely inelastic bouncing ball. *Phys. Rev. Lett.* **1990**, 65, 393-396.
- [62] Moon, S. J.; Shattuck, M. D.; Bizon, C.; Goldman, D. I.; Swift, J. B.; Swinney, H. L. Phase bubbles and spatiotemporal chaos in granular patterns. *Phys. Rev. E* **2002**, 65, 011301/1-10.
- [63] Umbanhowar, P. B. Wave Patterns in Vibrated Granular Layers. Ph. D. dissertation, The University of Texas at Austin, 1996.
- [64] Thomas, B.; Mason, M. O.; Squires, A. M. Some behaviors of shallow vibrated beds across a wide range in particle size and their implications for powder classification. *Powder Technol.* **2000**, 111, 34-49.
- [65] Gregor, W.; Rumpf, H. Velocity of sound in two-phase media. *Int. J. Multiphase Flow* **1975**, 1, 753-769.
- [66] Lätzel, M.; Luding, S.; Herrmann, H. J. Macroscopic material properties from quasi-static, microscopic simulations of a two-dimensional shear-cell. *Gran. Matt.* **2000**, 2, 123-135.
- [67] Rumpf, H. The strength of granules and agglomerates. in *Agglomeration*, ed. W. A. Knepper; Interscience; New York, 1962.

(a)



(b)

